

Nonlinear Simulation of Energetic Particle Modes in High-Beta Tokamak Plasma^{*})

Andreas BIERWAGE, Nobuyuki AIBA, Yasushi TODO¹⁾, Wenjun DENG²⁾,
Masao ISHIKAWA, Go MATSUNAGA, Kouji SHINOHARA and Masatoshi YAGI

Japan Atomic Energy Agency, Naka 311-0193, Japan

¹⁾*National Institute for Fusion Science, Toki 509-5292, Japan*

²⁾*University of California, Irvine CA 92697, USA*

(Received 2 December 2011 / Accepted 1 May 2012)

The effect of bulk pressure on the nonlinear dynamics of energetic particle modes (EPM) in a neutral-beam-driven JT-60U discharge is examined through nonlinear hybrid (MHD + particle) simulations with realistic values of the plasma beta and in realistic flux surface geometry. In the scenario studied, the linear EPM growth rate is 20% higher in the finite-beta compared to the zero-beta case, but compressibility stabilizes the mode by roughly the same amount. In the finite-beta case, the nonlinear frequency shift and the radial spreading/propagation of the mode are affected by the beta-induced gap in the shear Alfvén continuum. Although the evolution of the modes is affected by bulk pressure, compressibility and geometry, the overall energetic ion transport during the first few 100 Alfvén times following the saturation of the EPM is comparable in all cases studied.

© 2012 The Japan Society of Plasma Science and Nuclear Fusion Research

Keywords: high beta tokamak, shear Alfvén wave, energetic particle mode, nonlinear simulation, transport

DOI: 10.1585/pfr.7.2403081

1. Introduction

Burning tokamak plasmas will be characterized by high bulk plasma pressure and regions with steep pressure gradients. This raises the question how such a high-pressure state affects the interaction between the bulk plasma and energetic ions; which includes the excitation of Alfvénic modes and resulting transport of energetic ions. The purpose of this short paper is to summarize first nonlinear numerical simulation results obtained under such conditions.

This study considers shear Alfvén waves in the frequency range $\omega_{\text{BAE}} \lesssim \omega \lesssim \omega_{\text{TAE}}$, between the accumulation points of the beta-induced [1, 2] and toroidicity-induced gaps [3]. Simulations are carried out for cases based on the neutral-beam-driven JT-60U discharge E039672, where so-called abrupt large events (ALE) are observed [4,5]. These modes have frequencies in the range $40 \text{ kHz} \lesssim f \lesssim 60 \text{ kHz}$ and toroidal mode number $n = 1$, and cause significant energetic ion transport [4]. They are thought to be manifestations of $n = 1$ energetic particle modes (EPM [6]). Many features of such modes may be simulated by treating the bulk plasma as an MHD fluid that interacts with drift-kinetic energetic ions [7].

The three cases in Table 1 are compared, where β_{bulk} is the on-axis toroidal beta and Γ the specific heat ratio. The latter is used to control whether (“compressible”, $\Gamma > 1$) or not (“incompressible”, $\Gamma = 1$) work is done to keep the

author's e-mail: bierwage.andreas@jaea.go.jp

^{*}) This article is based on the presentation at the 21st International Toki Conference (ITC21).

Table 1 Cases studied and results of linear stability analysis.

case	parameters		linear eigenmode		
	β_{bulk}	Γ	label	γ	ω
1. cold, incomp.	0	1	(A)	0.041	0.20
2. warm, incomp.	3.6%	1	(D)	0.049	0.18
3. warm, comp.	3.6%	5/3	(G)	0.039	0.20

plasma volume constant while increasing β_{bulk} from zero to a finite value. Larger Γ means lower internal energy. Thus, in the following, the term “incompressible” is used in the thermodynamic sense ($\Gamma = 1$), which is different from incompressible flow ($\Gamma \rightarrow \infty$) and from the case where linear stability is independent of compressibility ($\Gamma = 0$). The results are used to verify high-beta effects in the code used (MEGA [8,9]) and obtain directions for further research.

2. Model

The equations describing the bulk plasma dynamics are

$$\rho_m \partial_t \mathbf{V} = -\rho_m \boldsymbol{\Omega} \times \mathbf{V} + (\mathbf{J} - \mathbf{J}_{\text{H,eff}}) \times \mathbf{B} - \nabla P \quad (1)$$

$$-\rho_m \left[\frac{1}{2} \nabla V^2 + \nu \nabla \times \boldsymbol{\Omega} - \frac{4}{3} \nu \nabla (\nabla \cdot \mathbf{V}) \right],$$

$$\partial_t \mathbf{B} = -\nabla \times \mathbf{E}, \quad (2)$$

$$\partial_t \rho_m = -\nabla \cdot (\rho_m \mathbf{V}), \quad (3)$$

$$\partial_t P = -\nabla \cdot (P \mathbf{V}) - (\Gamma - 1) P \nabla \cdot \mathbf{V} \quad (4)$$

$$+(\Gamma - 1) \left\{ \eta J^2 + \nu \rho_m [Q^2 + \frac{4}{3} (\nabla \cdot \mathbf{V})^2] \right\};$$

where \mathbf{B} is the magnetic field, $\mathbf{E} = -\mathbf{V} \times \mathbf{B} + \eta \mathbf{J}$ the

electric field, $\boldsymbol{\Omega} = \nabla \times \mathbf{V}$ the vorticity, $\mathbf{J} = \nabla \times \mathbf{B}/\mu_0$ the total current density. The energetic ion current density $\mathbf{J}_{H,\text{eff}}$ (excluding electric drift) is computed from the perturbed distribution function represented by phase space marker particles. The simulation setup is the same as the “shaped” case studied in Ref. [10]; except that the bulk density $\rho_m = m_i n_i$ and bulk pressure P are now evolved in time. The profiles of the safety factor $q(r)$ and toroidal bulk beta $\beta_{\text{bulk}}(r) = 2\mu_0 P(r)/v_{A0}^2$ are plotted in Fig. 1; where $r/a \in [0, 1]$ is the volume-averaged minor radius and $v_{A0} = B_0/(\mu_0 m_i n_i)^{1/2}$ the on-axis Alfvén velocity. The number of mesh points is $N_R \times N_\varphi \times N_Z = 152 \times 16 \times 128$, the number of markers is 2.1×10^6 , resistivity and viscosity are $\eta = 3 \times 10^{-6} \mu_0 v_{A0} R_0$ and $\nu = 10^{-6} v_{A0} R_0$. In the following, the time t is normalized by $\omega_{A0} = v_{A0}/R_0$. For further details about the model and code used, see Refs. [8, 9].

The energetic ions are set up as described in Ref. [10]. Note that $\beta_{H0} = 3.5\%$, so energetic and bulk ion pressures are comparable. For simplicity, an isotropic slowing-down model is used for the energetic ion equilibrium distribution function F_{H0} . This means that the total energetic particle energy is distributed over all pitch angles. Thus, for a given resonance, the drive is different (here, most likely weaker) than with an anisotropic distribution, which would represent conditions in beam-driven experiments more closely.

Only the perturbed $n = 1$ component of $\mathbf{J}_{H,\text{eff}}$ is included since the dominant fluctuations observed in the experiments have $n = 1$. Thus, only MHD nonlinearities transfer energy to $n = 0$ and $n > 1$ perturbations in the present simulations. However, this effect is found to be small here, so only $n = 1$ dynamics are discussed.

The choice to filter out $n \neq 1$ components of the energetic particle coupling term is justified as follows. The $n = 0$ equilibrium component is excluded since we are not yet capable of constructing a self-consistent equilibrium that takes into account the currents and pressures of bulk and energetic particles on equal footing. The evolution of the $n = 0$ perturbed component is excluded since it is known to be sensitive to kinetic effects of bulk particles, which are not captured by the MHD model. The exclusion of the $n > 1$ components avoids their resonant excitation, which may be caused by the present use of an isotropic model for F_{H0} instead of a more realistic anisotropic beam distribution. Similar arguments were previously put forward in Ref. [11]. It is expected that the main conclusions concerning energetic particle transport are not affected by

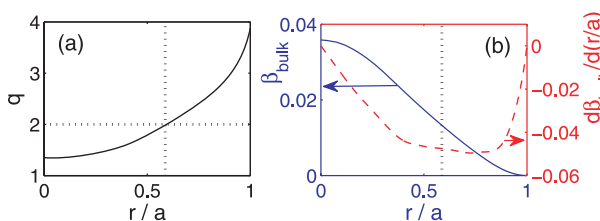


Fig. 1 Profiles of (a) safety factor, (b) bulk beta and its gradient.

the simplifications made. Research with more complex models will show whether this is indeed the case.

3. Results

In each case, three snapshots are taken to characterize the dynamics. They are labeled (A)-(C) in case 1, (D)-(F) in case 2 and (G)-(I) in case 3. Snapshots (A), (D) and (G) are taken during linear phase of each case, and the remaining snapshots characterize the nonlinear evolution. The linear growth rates and frequencies from Fig. 2 (a) and Fig. 3 (A,D,G) are summarized in Table 1.

Figure 2 shows the evolution of the $n = 1$ mode amplitude (square root of kinetic energy, $W = m_i n_i \int d^3 x |V|^2$). The incompressible finite-beta case (2.) has the highest growth rate and saturation amplitude. With zero beta (1.) the growth rate is about 20% lower and the saturation amplitude about 10% lower than in case 2. With compressibility included (3.) the growth rate and saturation amplitude are both reduced by about 20%. Qualitatively, these results are as expected from theory: in the first ideal MHD ballooning stable domain increasing bulk pressure is destabilizing, and compressibility is always stabilizing.

The power spectra in Fig. 3 show the frequency and radial location of the fluctuations. The linear mode structures (A,D,G) peak near $r \approx 0.45 \dots 0.5$, where the energetic ion pressure gradient is steepest. The mode frequencies lie in the range $\omega = 0.18 \dots 0.2$ and match the local frequency of the $m = 2$ continuum. The small differences between the three cases may be attributed to the differences in the continuous spectra, $\omega_{AC}(r)$. The slope of $\omega_{AC}(r)$ at the mode locations suggests significant continuum damping, so these modes have the character of a typical EPM.

The composition of the mode structure from the poloidal harmonics $m = 0 \dots 4$ is shown in Fig. 4. The $m = 2$ harmonic is dominant in the linear regime (A,D,G). The coupling to $m = 1$ and $m = 3$ harmonics is stronger with

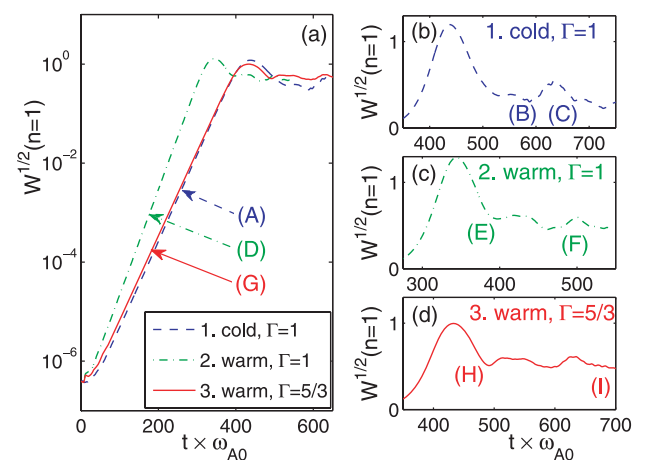


Fig. 2 Evolution of the $n = 1$ mode energy W : (a) log-scale plot and (b,c,d) linear-scale plots of the nonlinear evolution in the three cases studied. The labels (A)-(I) indicate times at which snapshots are taken (cf. Figs. 3-5).

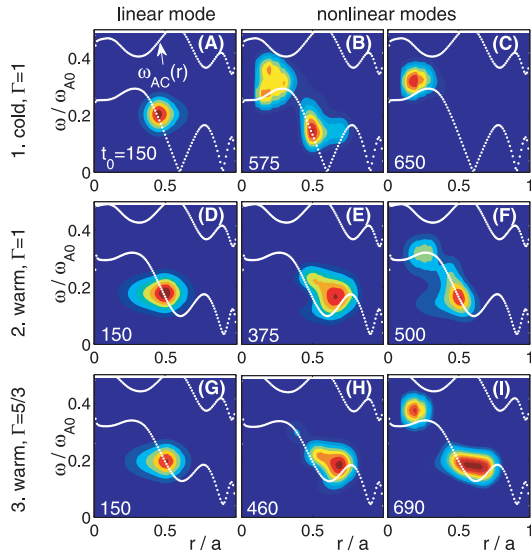


Fig. 3 Snapshot of the power spectrum contours of the electrostatic potential ϕ in the three cases studied. For the spectral analysis, a Hanning time window of width $100\omega_{A0}^{-1}$ around t_0 is used. Superimposed on the contour plots are lines indicating the continuous spectra $\omega_{AC}(r)$ [12] in the slow-sound approximation due to $\beta_{\text{bulk}} \ll 1$ [13]. The times at which snapshots (A)–(I) were taken are indicated by the numbers in the bottom-left corners (cf. Fig. 2).

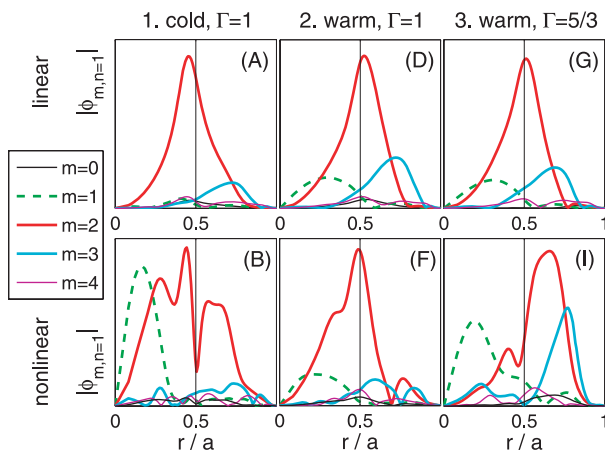


Fig. 4 Radial mode structure of the dominant poloidal harmonics $m = 0, 1, 2, 3, 4$ in the $n = 1$ component of the electrostatic potential $|\phi_{m,n}(r)|$ in the three cases studied. Three snapshots during the linear (A,D,G) and three during the nonlinear regime (B,F,H) are shown (cf. Figs. 2 and 3).

finite beta than with zero beta, which is as expected due to the effect of the pressure-curvature coupling term. Figure 5 shows the total mode structure in the poloidal plane.

Observations in the nonlinear phase are as follows. During the first and largest peak in the $n = 1$ mode amplitude plotted in Fig. 2 (b,c,d), the mode shifts downward in frequency and outward in minor radius. In doing so, the mode tends to follow the path prescribed by the continuous spectrum, $\omega_{AC}(r)$. Thus, in the finite-beta cases (2. and 3.), the frequency downward sweep terminates at the accumu-

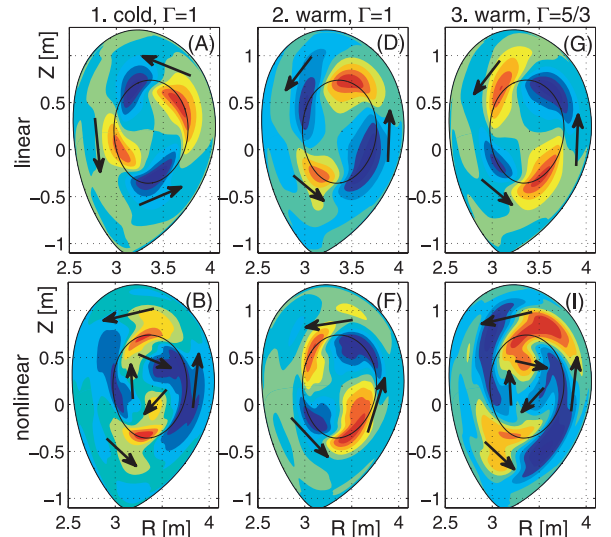


Fig. 5 Snapshot of the electrostatic potential $\phi_{n=1}(R,Z)$ mode structure contours in the three cases studied. Three snapshots during the linear (A,D,G) and three during the nonlinear regime (B,F,I) are shown (cf. Figs. 2 and 3). Arrows indicate the poloidal rotation of the structures.

lation point of the $m = 2$ BAE gap, $\omega_{BAE}(r = 0.63) = 0.15$, as may be seen in Figs. 3 (E) and (H). The mode follows the continuum across the $q = 2$ rational surface, from $r \approx 0.5$ to $r \approx 0.7$, and approaches the lower accumulation point of the $\{m, m'\} = \{2, 3\}$ TAE. In the zero-beta case (1.) the radial excursion of the mode is smaller, from $r \approx 0.45$ to $r \approx 0.55$, and the frequency drops deeper to $\omega \approx 0.13$, as shown by the lower peak in Fig. 3 (B).

Subsequently the modes in all cases (now at about 1/2 of their peak amplitude) show a tendency to move radially inward, following the continuous spectrum upward. The frequency may rise as far as the $\{m, m'\} = \{1, 2\}$ TAE accumulation point, $\omega_{TAE}(r = 0.22) = 0.34$, as in Fig. 3 (F). The dynamics become increasingly complex. Cycles of inward and outward motion of the mode, with up- and down-shifts in frequency, may continue and overlap, at amplitudes of about 1/3 to 1/2 of the peak amplitude [Figs. 2 (b,c,d)].

During this period, a second mode appears near the magnetic axis. The mode frequency is $\omega = 0.325$ in the zero-beta case, Fig. 3 (C), and $\omega = 0.375$ in the compressible finite-beta case, Fig. 3 (I). That is, ω is located about $\Delta\omega = 0.040$ above the local $m = 1$ continuum in both cases. Peaking in the region $0.16 \leq r \leq 0.21$, this mode is not radially aligned with the accumulation points of the toroidicity-induced gap, which are located at $r = 0.29$ in the zero-beta case (C) and $r = 0.26$ in the finite-beta case (I). Viewed in the poloidal plane, this centralized mode rotates in the opposite direction compared to the other modes, as indicated by arrows in Fig. 5 (B,I). During its nonlinear evolution in the zero-beta case, rapid (within 30 Alfvén times) up- and downward chirping of the mode frequency by $\pm(10\text{...}30)\%$ is observed. This mode and its

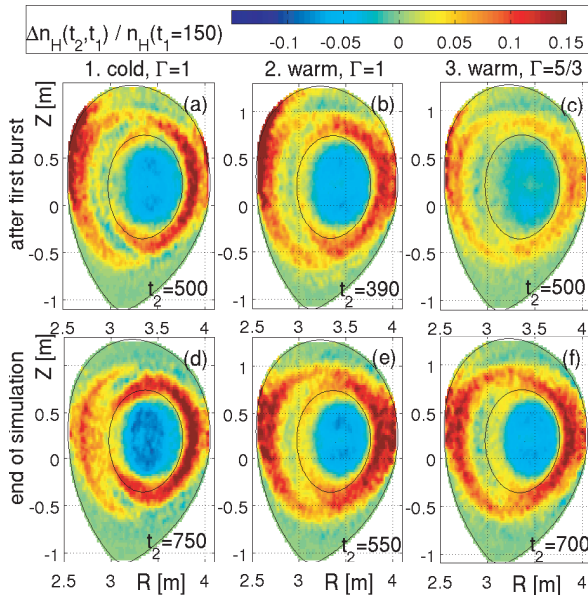


Fig. 6 Energetic ion density redistribution during the first two peaks of nonlinear $n = 1$ mode activity in (a,d) the zero-beta and (b,c,e,f) the finite-beta cases. (a,b,c) show the redistribution occurring during the first burst, (d,e,f) the cumulative redistribution at the end of the simulation.

properties remain to be understood.

The spatial redistribution of energetic ions due to the collective action of the modes described above is shown in Fig. 6, where the relative change in the velocity-space-averaged energetic ion density field is plotted. Here, the change in the density Δn_H is measured by subtracting the density field in the linear stage, $n_H(R, Z, t_1=150)$, from the density field computed at a later time, $t_2 > t_1$, and dividing this difference by $n_H(R, Z, t_1)$. The division by the reference field $n_H(R, Z, t_1)$ (not done in Ref. [10]) amplifies fluctuations near the boundary, where n_H is small. The change in the density field found after the major peak in $n = 1$ mode activity is shown in Fig. 6(a,b,c). Figures 6(d,e,f) show the situation another 160–250 Alfvén times later. During the major peak in mode activity, the values for Δn_H in cases 1 and 2 lie around $\pm(10\dots15)\%$, while it is only $\pm(5\dots10)\%$ in the compressible finite-beta case 3. However, while cases 1 and 2 stagnate, particle transport in case 3 continues until Δn_H also reaches $\pm(10\dots15)\%$. The transport processes as well as the structure of Δn_H seen in Fig. 6 remains to be clarified and quantified by analyzing the wave-particle interactions, the orbits of the displaced particles, and the fraction of lost particles.

4. Conclusion

The effect of bulk pressure on the nonlinear dynamics of energetic particle modes (EPM) observed in JT-60U discharge E039672 is examined. This work is the continuation of a series of simulations with increasing physical detail, starting with circular magnetic geometry and zero

pressure [14], considering realistic geometry [10] and now adding realistic bulk pressure in the fluid limit.

The results show clearly the effect of the shape of the continuous shear Alfvén spectrum (in particular, the BAE gap) on the evolution of the frequency and mode structure of the EPM. Enhanced poloidal mode coupling is also seen. Thus, these results serve as a verification of high-beta physics captured by MEGA.

In the nonlinear regime, only a time window of about 250 Alfvén times was examined. Beyond these first 250 Alfvén times, resistive ballooning instabilities (in particular, modes with $n \gtrsim 10$) and possibly numerical instabilities may begin to obscure the results. The long-term evolution will be studied carefully in future work.

A question of practical concern is how much transport is caused and where the displaced particles are deposited. Taking also into account the results of Ref. [10], where the effect of realistic non-circular magnetic flux surface geometry was studied, one may summarize the results obtained so far as follows: magnetic geometry and bulk pressure effects affect the linear stability and nonlinear evolution of EPM, but little effect on the overall energetic particle transport was seen with the diagnostics currently implemented in MEGA. In particular, the reduction of the energetic ion density in the central region of the plasma ($r/a \lesssim 0.5$) is similar in all cases studied. On the other hand, the radial distance over which particles are redistributed and the amount of particles that hit the wall may be more sensitive to the simulation setup. This will be examined after additional diagnostics are implemented in MEGA, allowing a detailed analysis of the particle transport. More accurate modeling of the boundary region may also be required.

The role of realistic modeling of the equilibrium distribution function will be examined next. The resonant nature of EPM [6] suggests that F_{H0} plays an important role.

Acknowledgments

This work was partly supported by Grant-in-Aid for Scientific Research from the Japanese Ministry of Education, Culture, Sports, Science and Technology, Grant No. 22860081. One of the authors (W.D.) was supported by U.S. Department of Energy SciDAC GSEP center.

- [1] W.W. Heidbrink *et al.*, Phys. Rev. Lett. **71**, 855 (1993).
- [2] A.D. Turnbull *et al.*, Phys. Fluids B **5**, 2546 (1993).
- [3] C.Z. Cheng *et al.*, Ann. Physics **161**, 21 (1985).
- [4] M. Ishikawa *et al.*, Nucl. Fusion **45**, 1474 (2005).
- [5] K. Shinohara *et al.*, Nucl. Fusion **41**, 603 (2001).
- [6] L. Chen, Phys. Plasmas **1**, 1519 (1994).
- [7] W. Park *et al.*, Phys. Fluids B **4**, 2033 (1992).
- [8] Y. Todo *et al.*, Phys. Plasmas **12**, 012503 (2005).
- [9] Y. Todo, Phys. Plasmas **13**, 082503 (2006).
- [10] A. Bierwage *et al.*, Plasma Fusion Res. **6**, 2403109 (2011).
- [11] G. Vlad *et al.*, Nucl. Fusion **49**, 075024 (2009).
- [12] W. Deng *et al.*, Nucl. Fusion **52**, 043006 (2012).
- [13] M. Chu *et al.*, Phys. Fluids B **4**, 11 (1992).
- [14] S. Briguglio *et al.*, Phys. Plasmas **14**, 055904 (2007).